The X-ray nebula around the type 2 Seyfert galaxy NGC 4388

K. Iwasawa,[1]★ A. S. Wilson,[2] A. C. Fabian[1] and A. J. Young[2]

[1]*Institute of Astronomy, Madingley Road, Cambridge CB3 0HA*
[2]*Department of Astronomy, University of Maryland, College Park, MD 20742-2421, USA*

ABSTRACT

We report on X-ray emission from the type 2 Seyfert galaxy NGC 4388 observed with the *Chandra* X-ray Observatory. A hard X-ray peak is found at the position of the active nucleus suggested by optical and radio observations. Extended soft X-ray emission correlates well with the ionization cone found in optical-line emission. A large soft X-ray extension is found up to 16 kpc (and possibly 30 kpc) to the north of the galaxy. Photoionized gas with low ionization parameters ($\log \xi \leqslant 0.4$) appears to be the likely explanation for this emission. The same ionized gas clouds could be responsible for the optical [O III] emission. Fe Kα line emission from cold material is found to be extended by a few kpc.

Key words: galaxies: individual: NGC 4388 – galaxies: ISM – X-rays: galaxies.

1 INTRODUCTION

NGC 4388 ($z = 0.008\,42$) is a nearly edge-on ($i \simeq 78°$) spiral galaxy hosting a type 2 Seyfert nucleus (Phillips & Malin 1982; Filippenko & Sargent 1985), located near the core of the Virgo cluster. The recession velocity measured for this galaxy (2540 km s^{-1}) is much higher than the cluster mean velocity (1100 km s^{-1}). This suggests that the galaxy is moving away from us through the intracluster medium (ICM) at a supersonic speed, and an interaction between the galaxy and ICM has been suspected, particularly in the context of ram-pressure stripping of the interstellar medium (Chamaraux, Balkowski & Gérard 1980; Giovanelli & Haynes 1983; Kenney & Young 1986; Petitjean & Durret 1993; Veilleux et al. 1999).

Radio images show a compact double central source and a plume extending to the north (Stone, Wilson & Ward 1988; Hummel & Saikia 1991; Falcke, Wilson & Simpson 1998). No broad emission component was found in optical spectropolarimetric observations of the nucleus (Kay 1994). However, the somewhat controversial detection of off-nuclear broad Hα emission by Shields & Filippenko (1988) led to the idea of an obscured type 1 Seyfert nucleus in NGC 4388. Unambiguous confirmation of the hypothesis came from hard X-ray observations by which a strongly absorbed ($N_{\rm H} \sim 10^{23}$ cm^{-2}) X-ray source has been detected (Hanson et al. 1990; Iwasawa et al. 1997; Bassani et al. 1999; Forster, Leighly & Kay 1999).

The presence of extended optical emission-line nebulae in NGC 4388 has been known for a few decades (Ford, Rubin & Roberts 1971; Sandage 1978; Colina et al. 1987; Corbin, Baldwin & Wilson 1988; Pogge 1988; Veilleux et al. 1999; Yoshida et al. 2001). Besides the low excitation optical emission extending along the galaxy disc, which probably traces active star-forming regions, the high excitation extended emission above the galactic plane has been of great

interest in connection with its kinematics and ionization mechanism. Until recently, the extraplanar ionized gas was known to extend up to 4 kpc from the nucleus, but the wide-field images obtained from the SUBARU SuprimeCam show optical filaments extending up to 35 kpc to the northeast (Yoshida et al. 2001). Studies of the excitation conditions in this extraplanar nebula suggest that it is likely to be photoionized by the central active nucleus, although some contribution by shock excitation has been claimed recently (Ciroi et al. 2003). The required ionizing luminosity is estimated to be of the order of 10^{43} erg s^{-1} (Kinney et al. 1991; Colina 1992; Yoshida et al. 2001).

The soft X-ray emission of NGC 4388 was first shown to be extended from a *ROSAT* HRI observation (Matt et al. 1994). However, the details of the extended X-ray emission and its origin have been unclear. In this paper, we present an imaging observation with the *Chandra* X-ray Observatory (Weisskopf et al. 2000), which reveals the detailed morphology of the extended X-ray nebula and spectral variations across the nebula, as well as the active nucleus seen in hard X-rays. The distance of the galaxy is assumed to be 16.7 Mpc throughout this paper. The angular scale is then ∼81 pc arcsec^{-1} (or 12 arcsec corresponding to 1 kpc).

2 OBSERVATION AND DATA REDUCTION

NGC 4388 was observed with the *Chandra* ACIS detectors on 2001 June 8. The nucleus of the galaxy was positioned on the ACIS-S3 detector. The focal plane temperature for this observation was −120°C. The data reduction was carried out using the CIAO 2.2 package and calibration files in CALDB version 2.10.

The data at the position of the nucleus of NGC 4388 are affected by photon pile-up (the estimated pile-up fraction is about 10 per cent). The detector background of ACIS-S3 during this observation was relatively stable. The analysis for the emission at small radii was

★E-mail: ki@ast.cam.ac.uk

© 2003 RAS

performed using the data of the full exposure of 20 ks. However, for extended emission found at larger radii, we filtered the event file using the 2.5–7 keV light curve from a source-free region on the S3 chip. Data taken in periods when the background counts deviate by more than 20 per cent from the mean value have been discarded, which results in an exposure time of 14 ks for analysis. The spectral analysis was performed using XSPEC version 11. The time-dependent degradation of the ACIS sensitivity at low energies has been corrected with ACISABS by Chartas & Getman.

The total background-corrected observed fluxes are estimated to be 3.4×10^{-13} erg cm^{-2} s^{-1} in the 0.5–2 keV band and 3.7×10^{-12} erg cm^{-2} s^{-1} in the 2–7 keV band.

3 ACTIVE NUCLEUS

The composite X-ray image of the central part of NGC 4388, produced from the three energy bands, 0.3–1 keV, 1–3 and 4–7 keV, is shown in Fig. 1. The active nucleus is located at the position of the hard X-ray peak indicated in blue. The soft X-ray emission shows complex morphology. Particularly bright is a conical feature to the south. These soft X-ray features are discussed in detail in the following section.

3.1 The hard X-ray nucleus

The active nucleus of NGC 4388 is very faint below 4 keV in the *Chandra* image and is not visible below 1 keV, due to obscuration probably associated with gas in the edge-on stellar disc.

Strong emission is seen at energies above 4 keV. Its spectral shape is consistent with a strongly absorbed source (Fig. 2). The spectrum presented in Fig. 2 was taken from within 1.5 arcsec radius of the hard X-ray peak. It can be broadly described as having a heavily absorbed power law above 3 keV with Fe K line features at 6.4 and near 7 keV and a flat component at low energies. As mentioned in Section 2, the nucleus is so bright that the data were affected by moderate photon pile-up (estimated to be ≈10 per cent). The main consequences of the photon pile-up are a hardening of the spectrum and a reduction in the detected flux. We correct for these effects using the pile-up model of Davis (2001).

The absorption column density is found to be $N_{\mathrm{H}} \simeq 3.5^{+0.4}_{-0.3} \times 10^{23}$ cm^{-2} (hereafter quoted errors are for a 90 per cent confidence range for one parameter of interest, unless stated otherwise), when
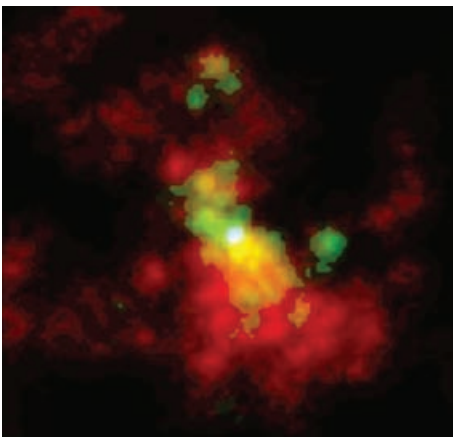

Figure 1. A composite X-ray image of the central part (45 × 43 arcsec² or 3.6 × 3.5 kpc²) of NGC 4388. The image has been constructed from three energy bands (red, 0.3–1 keV; green, 1–3 keV; blue, 4–7 keV). The active nucleus is located at the centre of the image, where the hard X-ray emission is peaked.
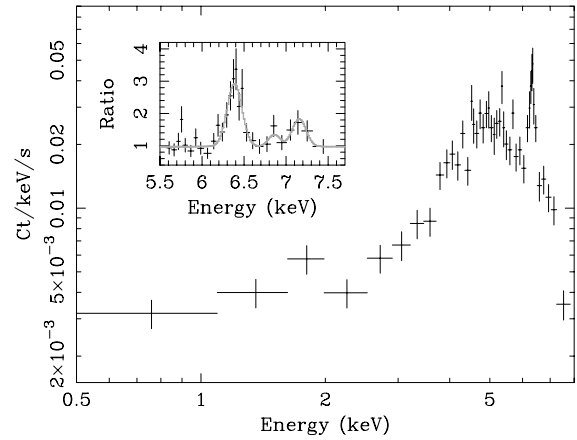

Figure 2. Main panel: the *Chandra* ACIS-S spectrum of the nucleus of NGC 4388, extracted from a region within 1.5 arcsec of the nucleus. The data are distorted by mild pile-up. A strong hard excess with an Fe K line is seen above 4 keV. The absorbing column density is estimated to be $N_{\mathrm{H}} \simeq 3.4 \times 10^{23}$ cm^{-2}, when $\Gamma = 1.8$ is assumed. Note that there is a faint, flat spectrum component below 4 keV. Inset: details of the Fe K band data in the form of a ratio of data and absorbed power-law model. The energy scale has been corrected for the galaxy redshift. The strong cold Fe Kα at 6.4 keV and weaker higher-energy line features are seen. The grey-line shows the best-fitting model including three gaussians, converted to the ratio form.

the photon index of the power-law continuum is assumed to be 1.8 and a simple absorbed power law is fitted to the 4–7.8 keV data. A deep Fe K photoelectric absorption edge seen above 7.1 keV is consistent with the large absorption column density.

A strong Fe Kα line is found at an energy of $6.36^{+0.02}_{-0.02}$ keV (hereafter quoted line energies are corrected for the galaxy redshift) with an equivalent width (EW) of EW = 440 ± 90 eV. The line flux is $(9.3 \pm 1.9) \times 10^{-5}$ photon s^{-1} cm^{-2}. This line is unresolved and the 90 per cent upper limit of the linewidth is FWHM ⩽ 23 500 km s^{-1}. There is also an excess peak at 7.1 ± 0.1 keV with EW = 200 ± 120 eV, and a less significant peak at ≃6.8 keV with EW ≃ 60 eV (90 per cent confidence detection). The estimated line fluxes for these lines are ≃2.7 × 10^{-5} and ≃1.2 × 10^{-5} photon s^{-1} cm^{-2}, respectively. Given the low pile-up fraction, these weak emission features (at least the statistically robust one at 7.1 keV) are unlikely to be artefacts of pile-up. A similar feature was detected at 6.9 ± 0.1 keV in the *ASCA* SIS spectrum. Fe Kβ emission is predicted to be three times weaker than the observed value. It could be blended with Fe XXVI Kα at 6.97 keV from a highly ionized medium. A similar Kα line from hydrogen-like iron has been detected in the *XMM–Newton* spectrum of the type 2 Seyfert galaxy Mrk463 (Sanders et al., in preparation). The presence of such a highly ionized Fe line is consistent with the high-ionization (log ξ ~ 3) component of the gas hypothesized for the southern cone in Section 4.1.

Extrapolating the absorbed power law leaves a faint excess below 4 keV. The spectrum is nearly flat, with $\Gamma = -0.3^{+0.5}_{-0.6}$ in the 0.5–2 keV band. This component is probably scattered light of the hidden active nucleus. As the soft X-ray image shows, the nucleus is very faint below 1 keV, suggesting further obscuration to the scattering region, in addition to the primary obscuration of the central source occurring probably at much smaller radii.

The observed fluxes (corrected for pile-up) in the 0.5–2 and 2–7 keV bands are 2.1 × 10^{-14} and 2.7 × 10^{-12} erg cm^{-2} s^{-1}, respectively. The estimated absorption-corrected 2–10 keV luminosity, excluding the iron line luminosity, is 6.3 × 10^{41} erg s^{-1}. This value

is lower than the two previous *ASCA* observations in 1993 and 1995 (Iwasawa et al. 1997; Forster et al. 1999) by a factor of 2–3.

3.2 Position of the active nucleus

The obscuration of the nuclear region affects the measurements of the position of the optical nucleus of this galaxy. The northern blob of the central double radio source has been considered to be the active nucleus, since it has a flat spectrum (Carral, Turner & Ho 1990). The best registration of the radio and optical images obtained so far is that by Falcke et al. (1998, see the paper for a detailed discussion) for the VLA and *Hubble Space Telescope* (*HST*) data. The positions of the *HST* red peak and the northern blob in the VLA 3.5-cm map are in agreement to within 0.45 arcsec. Our 4–7 keV image shows a strong point-like source with a faint envelope. In this energy band, the nucleus is largely free of obscuration and its position should coincide with the active nucleus. We have applied the latest aspect correction using the alignment files released in 2002 May by the *Chandra* Science Centre. With this aspect correction, the expected absolute positional accuracy is smaller than 0.6 arcsec. Our 4–7 keV peak is located at RA = $12^h25^m46\overset{s}{.}77$, Dec. = $+12°39'44''.0$ (J2000), which is ≈0.6 arcsec NE of the VLA radio nucleus. Given the uncertainties, the optical, radio and the X-ray positions are all in agreement.

4 SOFT X-RAY NEBULA

The soft X-ray emission is spatially extended and shows an interesting morphology. The 0.3–1 keV image of the central 2×1.65 arcmin^2 or 9.7×8.0 kpc^2 is shown, along with the X-ray colour map (0.7–1 keV/0.4–0.7 keV) in Fig. 3. Some regions of interest are investigated separately below. Basic data for these regions are summarized in Table 1.

4.1 Southern cone

The soft X-ray (0.3–1 keV) image shows a well-defined conical extension to the south (Figs 1 and 3a), resembling the [O III]λ5007 ionization cone (Pogge 1988; Falcke et al. 1998; Veilleux et al. 1999; Yoshida et al. 2001). The western side of the soft X-ray cone, in particular, has a sharp, straight boundary at PA ≈ 220°. Its apex is, however, slightly north of the hard X-ray peak. With the apex of the cone slightly displaced from the nuclear position (0.5 arcsec to the east, 2.5 arcsec to the north) when extrapolated with the rims of the cone, the opening angle of the X-ray cone is measured to be ≈55°.

The surface brightness of the soft X-ray emission drops at the centre due to strong absorption, whilst at radii greater than 2 arcsec from the nucleus, where the brightness peaks, its profile shows an exponential decline ($\propto \exp[-(r-2.6)/3.9]$, where r is the radial distance from the hard X-ray nucleus in arcsec). An alternative description is with a King profile with a core radius of 5.7 arcsec (or 460 pc) and a slope index of -1.7. In either case, the soft X-ray emission reaches the background level at radii of 20–25 arcsec (1.6–2 kpc), and there appears to be no further emission at larger radii to the south (in contrast to the northerly direction; see the following section).

The ACIS-S spectrum of the southern cone is shown in Fig. 4. The spectral data were taken from a conical region in the radial range of 1.5–19 arcsec from the nucleus. The spectrum is dominated by soft X-ray emission below 3 keV.

Although the steep rise of the soft X-ray spectrum down to 0.5 keV can be approximated by a power-law form with a photon index of Γ ∼ 3.4, the most likely explanation for the soft X-ray emission is a blend of strong emission lines. Modelling by thermal emission spectra (from collisionally ionized plasma, e.g. MEKAL, Kaastra 1992) is not favoured on the following grounds. If the observed X-ray emission is due to collisionally ionized plasma, a likely origin is a galactic outflow driven by a nuclear starburst. Circumstantial evidence against this hypothesis is that, although star formation is taking place in the spiral arms of the stellar disc (Pogge 1988), there is no strong evidence for a compact nuclear starburst in NGC 4388. To drive a well-collimated outflow, as seen in the southern cone, a compact starburst region needs to be thermalized to form a high-pressure core (e.g. Chevalier & Clegg 1985), which does not appear to be the case in NGC 4388.

Spectral analysis does not support the thermal emission hypothesis either. A single temperature model fails to explain the strong
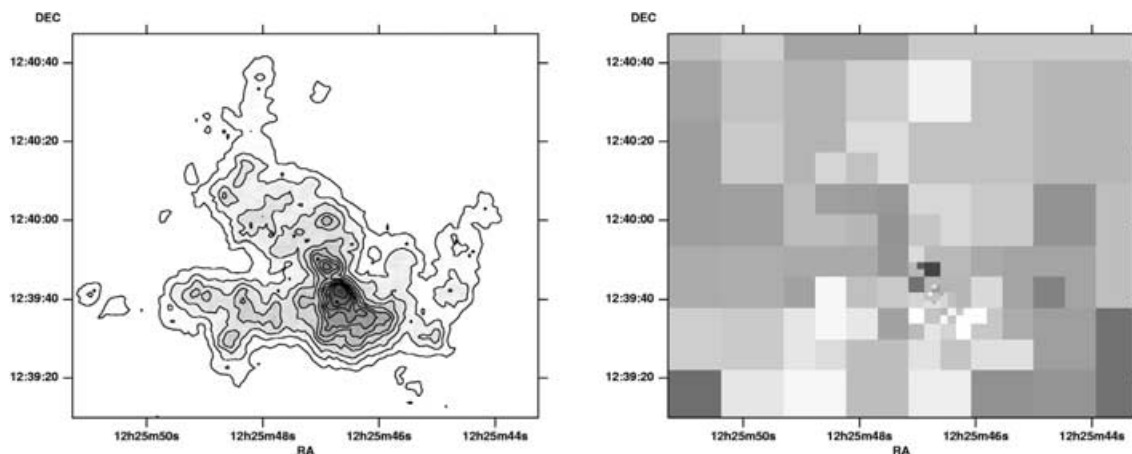
Figure 3. (a) Left-hand panel: the soft X-ray (0.3–1 keV) image of NGC 4388 (2×1.65 arcmin^2: 9.6×8.0 kpc^2). The sky coordinates are of J2000. The contours are drawn at 10 logarithmic intervals in the range of 0.5–50 per cent of the peak flux, which occurs at the inner part of the southern cone. (b) Right-hand panel: the hardness ratio image of the same field as the left-hand panel. Count rate ratios, $C(0.7–1\text{ keV})/C(0.4–0.7\text{ keV})$, are indicated on a logarithmic scale between 0.01 and 10 (the darker the shade, the larger the count rate ratio). The hardest spectrum occurs at the north plume near the nucleus. The three-shell region to the northeast (Section 4.3) has a relatively hard spectrum. The southern cone and the eastern extension along the stellar disc show a softer spectrum on average while there is evidence for some variations within the region.

Table 1. Selected regions for analysis of extended X-ray emission. Energy spectra for these regions are presented in Figs 4 and 10. S cone, a conical region to the south of the nucleus in the radial range of 1.5–19 arcsec from the nucleus; N plume, a region of 1.5–12 arcsec to the north of the nucleus; LSB, low surface brightness region consisting of the NE three-shell region (see Section 4.3), the galactic ridge to the east, and the western ridge seen in Fig. 3; and VLSB NE: a region to the northeast for the very low surface brightness emission (see Fig. 8) in the radial range of 50–110 arcsec. The fluxes given below are as observed (corrected only for the efficiency degradation of the ACIS detector).

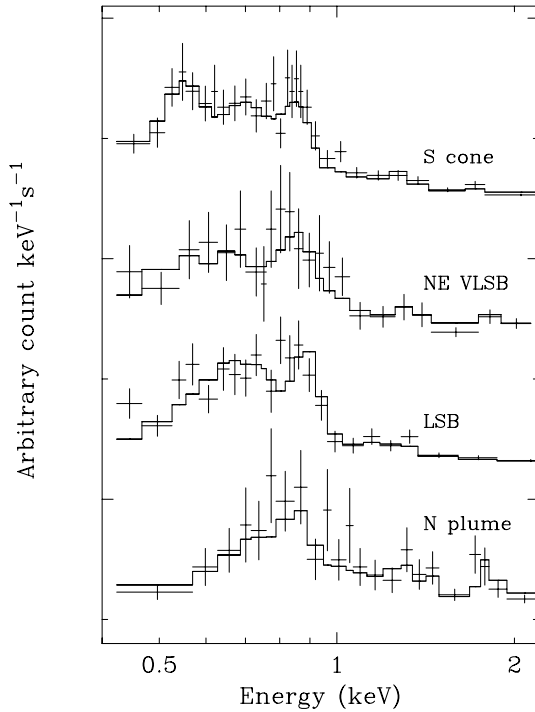| Region	Area (arcmin^2)	Count rate (10^{-2} count s^{-1})	$F_{0.5-2\,\text{keV}}$ (erg cm^{-2} s^{-1})	$F_{2-4\,\text{keV}}$ (erg cm^{-2} s^{-1})
S cone	0.062	4.02 ± 0.14	11.4×10^{-14}	2.9×10^{-14}
N plume ($r \leqslant 1$ kpc)	0.021	1.09 ± 0.07	2.5×10^{-14}	2.4×10^{-14}
LSB ($r \approx 1$–4 kpc)	0.58	3.17 ± 0.15	8.3×10^{-14}	2.0×10^{-14}
VLSB NE ($r \approx 4$–9 kpc)	1.10	1.32 ± 0.14	4.2×10^{-14}	–

Figure 4. The soft X-ray spectra (the *y*-axis has a linear scale) taken from the southern cone, the northeast very low surface brightness (NE VLSB) emission, the low surface brightness emission within 4 kpc and the northern plume within 1 kpc (from top to bottom). Information on each region is summarized in Table 1. To compare the relative strengths of spectral features in the spectra, they have been normalized to the emission peak at 0.8–0.9 keV and an arbitrary offset added for clarity. Note the strong O VII line at 0.55 keV in the S cone spectrum and the absorbed flat spectrum for the N plume. The solid-line histograms indicate possible models of emission from photoionized gas, for which details are given in the text.

O VII emission lines at 0.56 keV, even with a non-solar abundance ratio. Strong O VII is emitted from $kT \simeq 0.15$ keV gas if it is collisionally ionized. Since this low-temperature gas does not emit much above 0.7 keV, a higher-temperature gas is required to explain the data. A two-temperature model in which one component has a fixed temperature of $kT_1 = 0.15$ keV and the other has a fitted temperature of $kT_2 = 0.53^{+0.07}_{-0.07}$ keV gives a reasonable fit to the data up to 1.5 keV with $\chi^2 = 30.1$ for 39 degrees of freedom. This fit, however, underestimates the Mg emission feature at 1.3 keV by a factor of 2, and the Si feature at 1.8 keV by a factor of 4, on extrapolation. This

modelling also has two other significant problems: (1) the metallicity, which is assumed to be identical between the two components, is very low, $0.08^{+0.14}_{-0.06}$ solar. Such metallicity is unreasonable for gas in the central kpc of a spiral galaxy; (2) large internal absorption of $N_{\text{H}} = 2.4^{+1.6}_{-1.5} \times 10^{21}$ cm^{-2} is required. With the Galactic dust-to-gas ratio, this implies a visual extinction of $A_V \simeq 2.2$ mag. Unlike the northern extension (see Section 4.2), the southern cone is located well outside the obscuration and such a large extinction is unlikely to be present (even the nuclear optical spectrum taken from inner radii shows a smaller extinction $A_V \simeq 0.9$, Petitjean & Durret 1993).

We therefore explore the possibility of a photoionized plasma, as postulated for the optical ionization cone. In terms of quality of the fit to the data, the photoionization model described below gives a better fit to the data in the same energy range (0.4–1.5 keV) with $\chi^2 = 19.1$ for 40 degrees of freedom.

High-resolution X-ray spectra of photoionized gas in type 2 Seyfert galaxies obtained from grating spectrometers show many emission features from a broad range of ionization in the soft X-ray band (e.g. see Kinkhabwala et al. 2002; Brinkman et al. 2002, for *XMM–Newton* RGS and *Chandra* LETGS data, respectively, of NGC 1068; Sako et al. 2000 for Mrk 3). These emission lines are heavily blended together and mostly difficult to resolve at the spectral resolution of the CCD. This heavy line blending also makes an estimate of the underlying continuum difficult in a CCD spectrum, if it is present at all. Therefore, we will not perform a detailed analysis here as one would accomplish with a high-resolution grating spectrum, but instead only describe some key features characterizing the observed spectrum and present a possible model, which should be treated as a guide only.

A few of the strongest emission-line peaks can be recognized in the data at 0.56, 0.86, 1.33, 1.77 and 2.33 keV, for which the typical error in the line centroids is 0.04 keV and the significance of the detection is larger than the 90 per cent confidence level. These correspond to the O VII triplet, a blend of various Fe L emission, O VIII radiative recombination continuum (RRC) and Ne IX (0.92 keV), and low ionization (IV–VIII; for the ionization parameter inferred below) lines of Mg, Si and S, respectively. These are all low ionization features, and the 0.4–0.9 keV data and the three discrete emission lines above 1 keV are explained well with emission from optically thin gas with log $\xi \simeq 0.4$ (here, we compare with model spectra generated by XSTAR version 2.1 by T. Kallman, see Kallman & Bautista 2001, for optically thin gas, illuminated by a power-law continuum between 13.6 eV and 50 keV with a photon index of 1.8). The ionization parameter is defined as $\xi = L/(nR^2)$ erg cm s^{-1}, where L is the 1–1000 Ryd luminosity, n is the density and R is the distance from

the ionizing source. XSTAR was used to calculate the physical conditions in a spherical shell of gas by solving radiative transfer. The quoted value for ξ is for the inner edge of the shell. Therefore, the calculated spectra include emission from a range of ξ lower than the quoted value from outer radii. This fit requires no significant excess absorption by cold gas above the Galactic value ($N_H = 2.6 \times 10^{20}$ cm^{-2}, Dickey & Lockman 1990). The only significant residual below 0.9 keV is an excess at 0.65 keV, which could be O VIII Lyα, indicating the presence of higher ionization gas.

The 0.9–3 keV data unexplained by this model with $\log \xi \simeq 0.4$ emission, apart from the Mg, Si and S emission lines, may be emission and scattered continua from highly ionized, low-density gas, as suggested by the excess O VIII emission at 0.65 keV. Unfortunately, there is no other significant detection of spectral signatures, which could be used to constrain the ionization parameter. If Fe XXV at 6.7 keV, possibly present in the hard X-ray spectrum (see Section 5.1), is real and originates from the same medium as the O VIII emission, then the ionization parameter ξ would be a few thousand. For example, the spectrum from high ionization gas with $\xi = 2000$, when combined with the low ionization ($\log \xi = 0.4$) spectrum, can provide a reasonable fit to the 0.4–3 keV data (see Fig. 4). This high ionization spectrum has broader radiative recombination continua due to high temperature of the gas ($T \sim 10^6$ K), as well as high ionization lines, which could fill the continuum between the emission lines of the low ionization spectrum. A possible alternative which would play the same role is the soft X-ray excess component of the reflection spectrum, which is seen in the hard X-ray band (see, e.g., Ross, Fabian & Young 1999 for a computed reflection spectrum from mildly ionized matter). Further investigation is, however, beyond the capability of the present CCD spectrum.

In summary, low ionization ($\log \xi \simeq 0.4$) photoionized gas appears to be a plausible explanation for prominent soft X-ray spectral features. Another component, which could be highly ionized ($\log \xi \simeq 3$) gas, is required, although its origin is not clear. It should, however, be noted that this two-component photoionization model is only an approximation required to describe the spectrum at the CCD resolution with a limited signal-to-noise ratio, from which only a few strong emission features can be recognized. Emission features from photoionized gas with a broad range of ionization parameter are likely to be present and would be detected in a high-resolution spectrum.

There are significant spectral changes within the southern cone (see Fig. 3b). We compare spectra from radial ranges of 1.5–7 arcsec (0.1–0.6 kpc) and 7–19 arcsec (0.6–1.5 kpc); note that the maximum [O III]/Hα ratio occurs at 3 arcsec from the nucleus (Falcke et al. 1998; Veilleux et al. 1999). At the low-energy end, the spectrum from the larger radii is slightly softer than that from the inner part. The spectral softening at larger radii can be explained by a slight increase in ionization parameter for the low ionization gas, or a decrease in absorption, or both. In the second case, with a constant ionization parameter of $\log \xi = 0.4$, slightly larger absorption ($N_H \approx 2 \times 10^{20}$ cm^{-2}) than the Galactic value is found for the inner part, while no excess absorption is required for the outer part.

4.2 Northern extension within 1 kpc

In contrast to the southern extension, the inner part on the north side of the nucleus (within ~15 arcsec or 1.2 kpc) is faint in the soft X-ray (0.3–1 keV) band. However, the appearance of the image changes dramatically at higher energies. In the 1–2 keV band, the northern and southern extensions show comparable brightness, except very

close to the nucleus (Fig. 5). This is also demonstrated by radial profiles in the two energy bands (Fig. 6).

This change in appearance of the X-ray image can be understood as a result of obscuration toward the northern extension (and the
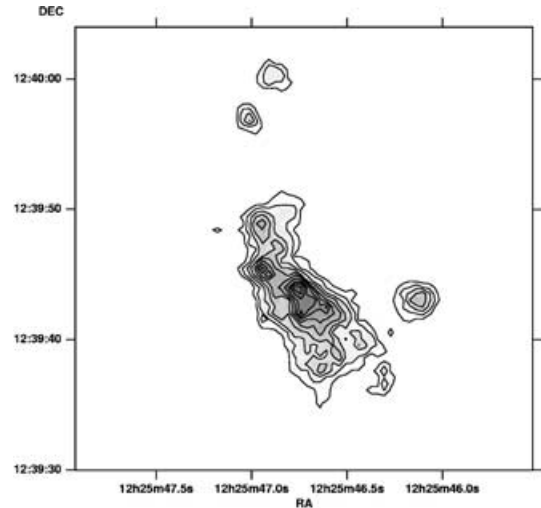

Figure 5. The 1–2 keV image of the central part of NGC 4388. The active nucleus is located at the central peak. The contours denote nine logarithmic intervals in the range of 0.15–80 per cent of the peak brightness.
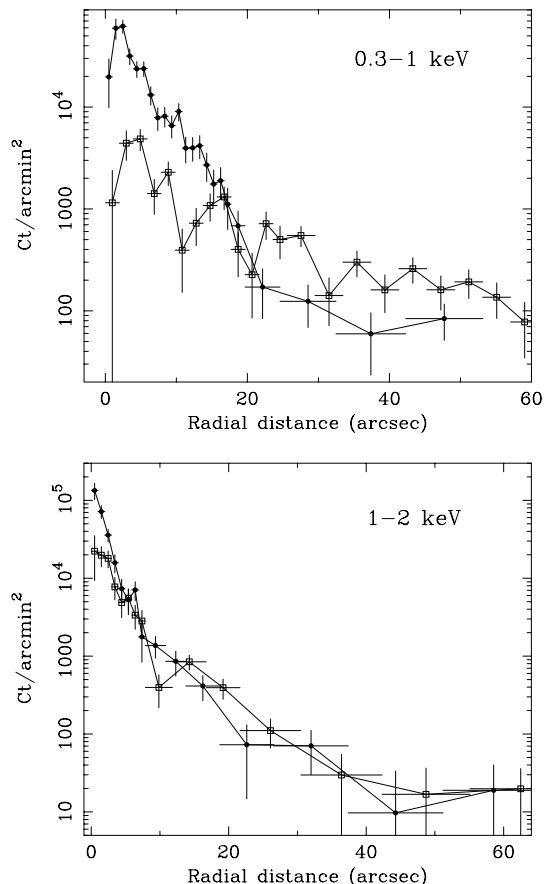

Figure 6. The surface brightness profiles of the NE (Open squares, PA = 355°–75°) and SW (Filled circles, PA = 165°–225°) cones in the 0.3–1 keV (upper panel) and 1–2 keV (lower panel) bands.

nucleus). The soft X-ray spectrum taken from the radial range of 3–11 arcsec (0.2–0.9 kpc) to the north of the nucleus is shown as 'N plume' in Fig. 4. In comparison with the southern cone spectrum, the soft X-ray excess below 0.9 keV is much less pronounced, and the low ionization emission lines from Mg and Si in the 1–2 keV range are stronger relative to the emission complex at lower energies. The data can be modelled by the same combination of low and high ionization gases as used for the southern cone spectrum (see Section 4.1) but with a larger absorption column density of $N_H = 2.1^{+0.6}_{-0.5} \times 10^{21}$ cm^{-2} (the model is shown as a solid histogram together with the data in Fig. 4). Combining with the radial surface brightness profiles in Fig. 6, it can be argued that, in the absence of absorption, the nebulae to the north and south would share similar brightnesses and possibly ionization conditions.

NGC 4388 is viewed nearly edge-on, with the near side of the stellar disc being tilted upward by ∼12° (see fig. 5 of Veilleux et al. 1999). This enables us to have a clear view of the SW cone. On the other hand, the tilted near side of the disc blocks our line of sight towards the northern extension, suppressing low-energy X-ray emission through photoelectric absorption. Probably we see the northern extended X-ray emission through the stellar disc for which the inferred column density appears to be reasonable.

There are a few morphological and spectral features to note on the northern extension: the 1–2 keV image (Fig. 5) shows that a relatively narrow bright filament emanates from the nucleus at PA ≈ 55° before bending northwards at ∼3 arcsec from the nucleus, past which point the filament opens up, similar to the radio plume imaged with the VLA (Falcke et al. 1998).

4.3 Lower surface brightness emission within 4 kpc

Besides the bright southern cone and the northern extension at small radii, lower surface brightness soft X-ray emission is seen in the radial range of 1–4 kpc from the nucleus. The extension is to the east along the stellar disc, to the west with a bent morphology, and to the northeast, as shown in Fig. 3(a). Although there is possible evidence for spectral variations across the low surface brightness emission (Fig. 3b), limited statistics due to the short exposure of our observation prevent us from dividing the low surface brightness emission into multiple regions and analysing their spectra separately. The soft X-ray spectrum integrated over this region is shown in Fig. 4 as 'LSB'.

Although, as cautioned above, the photoionization model should be taken as only a guide, the spectrum favours a higher ionization parameter of $\log \xi \simeq 1.4$ for the low ionization gas than that for the southern cone. A large absorption of $N_H = 2.5^{+0.9}_{-0.8} \times 10^{21}$ cm^{-2} is required. It should also be noted that the emission extended along the stellar disc might be different in origin. As the optical Hα image and the excitation map (Corbin et al. 1988; Veilleux et al. 1999; Yoshida et al. 2001) show, this region is the site of intense star formation in the spiral arms, and the soft X-ray emission could originate in thermal hot gas with a temperature of a few million K. The spectrum of the LSB lacks the strong O VII feature at 0.55 keV, but the quality of the present data cannot provide a clear answer to the question of whether the gas is collisionally ionized or photoionized.

To the northeast, the soft X-ray image shows three shell-like structures, aligned parallel to each other with an approximate separation of 10 arcsec, or 0.8 kpc (Fig. 7). They are located in the radial range of 14–40 arcsec (1.1–3.2 kpc) from the nucleus at PA ≃ 40°, and coincide with the location of the [O III] northeast complex (e.g. Veilleux et al. 1999). The colour map (Fig. 3b) shows that the three-
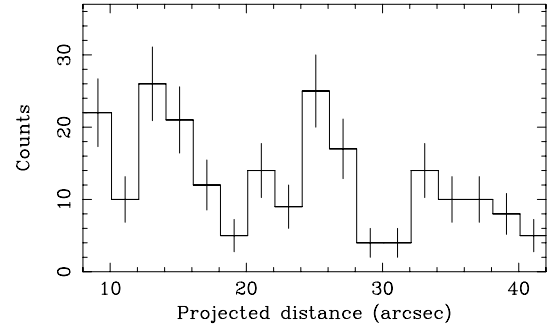
Figure 7. The projected surface brightness profile of the three shells seen in the 0.3–1 keV image (Fig. 3) to the northeast. The *x*-axis denotes the angular distance from the nucleus in PA = 38°. The detected counts are integrated over a 25-arcsec wide strip for each bin (the bin width is 2 arcsec). Three peaks are seen at around 14, 25 and 35 arcsec in projected distance.

shell region has a harder spectrum than the surroundings. In fact, the shell structure is clearer in the 0.7–1 keV image than in the 0.4–0.7 keV image.

4.4 Northern extension beyond 4 kpc

The large-scale image in the 0.3–2.5 keV band is shown in Fig. 8. The original image was produced from the entire ACIS-S3 chip with 5-arcsec binning. In this energy band, the Virgo cluster emission is significant. The background obtained from a source-free region on the same detector was assumed to be constant over the field. After subtracting the background, the image has been adaptively binned so that each pixel has a signal-to-noise ratio larger than 2.5.

Very low surface brightness emission extends to the northeast beyond the region shown in Fig. 3. There is a low-sensitivity belt on the detector due to the CCD node boundary, which extends in PA ≈ 120° at around 1.8 arcmin (∼9 kpc) from the nucleus. Including this sensitivity gap, extended emission with significance above 3σ reaches 3.3 arcmin (∼16 kpc) from the nucleus. It coincides with the region where emission-line filaments are seen in both the Hα
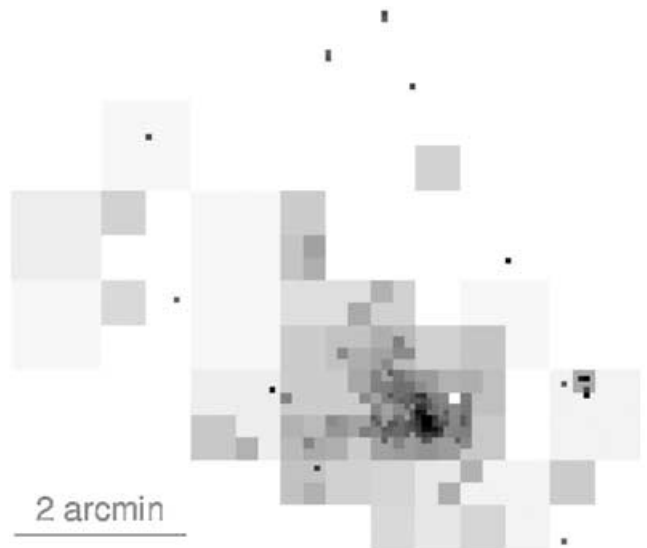
Figure 8. The large-scale soft X-ray (0.3–2.5 keV) image of NGC 4388. The background-subtracted 5-arcsec bin image has been adaptively binned to show faint, large-scale structures. Dark dots scattered over the region are mostly point sources.

and [O III] images taken by the SUBARU SuprimeCam (Yoshida et al. 2001).

The radial surface brightness profile of the 0.3–2.5 keV emission to the northeast (in the PA range between 0° and 50°) can be fit well with a power law ($\propto r^{\alpha}$; r in kpc) with $\alpha = -1.39 \pm 0.06$. A fainter excess is seen further out at PA $\sim 45°$, 4 arcmin (20 kpc) away from the nucleus, where there is a bright complex of Hα knots, which is a part of the SUBARU 35-kpc-long filament (Yoshida et al. 2001). However, the significance of this X-ray excess is just above 2σ.

The spectrum taken from the region between 4 and 9 kpc in radius is shown in Fig. 4 (as 'NE VLSB'). No significant emission is detected above 2 keV. Two prominent emission lines from low ionization Mg and Si at 1.3 and 1.8 keV, respectively, are seen in the 1–2 keV range. The inferred ionization parameter is found to be low at $\log \xi \simeq 0.3$, assuming Galactic absorption.

5 HARD X-RAY EMISSION

5.1 Circumnuclear hard X-ray emission

The 4–7 keV emission is highly concentrated around the nucleus (approximately 90 per cent of the total 4–7 keV flux comes from the central 2 arcsec in radius) but marginally resolved. The surface brightness distribution of the hard X-ray emission is found to be skewed slightly to the north at low brightness levels (see also the following subsection on the Fe Kα emission). The asymmetry suggests that the extension is real. Since the point spread function (PSF) of the *Chandra* optics (HRMA) has a broad low-level wing at high energies, we have examined the radial distribution of the hard X-ray emission. Fig. 9 shows radial surface brightness profiles in the 4–7 keV band, taken from northern and southern regions separated at PAs of 80° and 255° to compare with the PSF (note that the north-
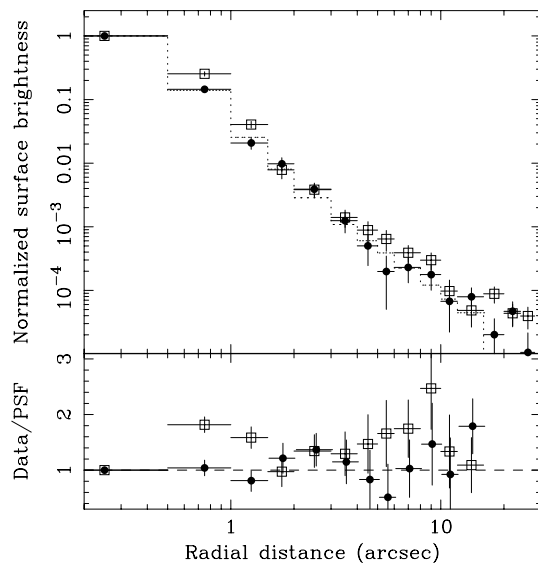
ern region overlaps the southern cone slightly at its inner western edge). We note that the photon pile-up at the nucleus results in a slightly diluted core. The innermost bins of the two observed profiles have been increased by 10 per cent as an approximate correction for pile-up.

A PSF was simulated at a monochromatic energy of 6.4 keV for the same position on the detector as that of the hard X-ray nucleus, using the standard PSF library in CIAO. The total hard X-ray spectrum peaks at the Fe Kα band (6.1–6.6 keV), which carries $\simeq 20$ per cent of the observed 4–7 keV counts. Because the off-axis angle of the source is small (0.65 arcmin) and 6.4 keV is close to the higher end of the bandpass, the simulated PSF can be regarded as a conservative estimate of the PSF for the 4–7 keV emission. While the radial profile for the southern half is consistent with the PSF, the northern half shows significant excess emission above the PSF but reaches the background level at around 30 arcsec ($\sim$2.5 kpc).

The origin of the extended hard X-ray emission is probably some form of reflection of the hidden active nucleus, as suggested by the hard spectrum (Fig. 10). This appears to be true, at least, for the spectrum of the low surface brightness emission region, which shows a strong Fe K line at 6.35 ± 0.06 keV with EW = 1.8 ± 0.9 keV. A similar picture is consistent with the noisy spectrum of the inner northern plume, which barely shows evidence for an Fe K line with EW = 770 ± 610 eV. This cold reflection could contribute to low ionization lines at lower energies (e.g. 2–4 keV band), depending on the ionization state and obscuration to the reflecting medium.
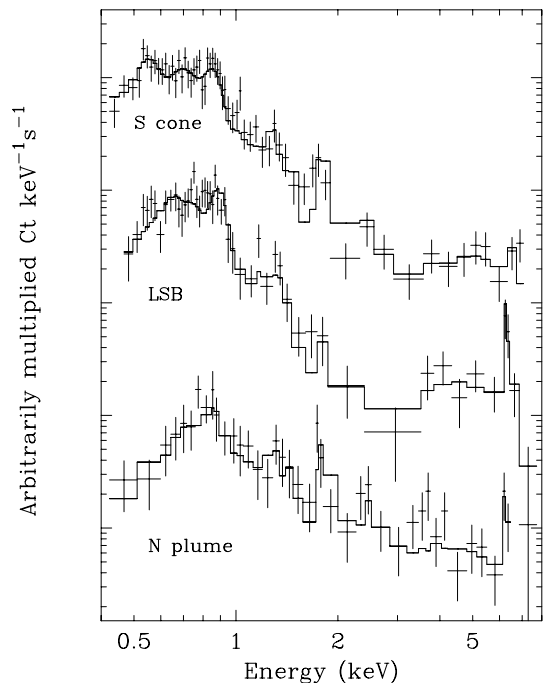
Figure 9. Upper panel: surface brightness profiles of 4–7 keV emission taken from PA ranges of 255°–80° (open squares) and 80°–255° (filled circles). The radial distance is measured from the position of the hard X-ray nucleus. The innermost bins of the profiles have been corrected for pile-up (by 10 per cent), and the data are normalized to the corrected innermost bins. The dotted-line histogram shows a simulated PSF of monochromatic 6.4-keV X-rays (note that the PSF profile is truncated at 15 arcsec). Bottom panel: ratios of the data of the two radial profiles to the PSF. The profile for the southern PA region is consistent with the PSF, while that of the northern PA region is broader than the PSF.

Figure 10. Full-band ACIS spectra (both *x*- and *y*-axes have logarithmic scales) of the southern cone, low surface brightness emission within 4 kpc, and the inner north plume (from top to bottom). All the three regions show weak hard X-ray tails in their spectra. It should, however, be noted that the hard tail in the S cone spectrum could be largely due to the scattered wing of the nuclear source PSF (see Section 5). No significant hard X-ray emission above 2 keV is detected at radii larger than 4 kpc. Solid-line histograms show fitted models including a reflection continuum (and a Fe K line where applicable) in the hard band in addition to those for photoionized gas emission for the soft X-ray band, presented in Fig. 4. Note the strong Fe K line at 6.4 keV in the LSB spectrum in contrast to the lack of such a strong line in the southern cone spectrum.

The reflecting medium could be molecular clouds distributed in the stellar disc (recall the Sgr B2 clouds near our galactic centre, which are located 100 pc away from Sgr A*, e.g. Koyama et al. 1996). If ram-pressure stripping of the gas in the host galaxy is taking place (e.g. Petitjean & Durret 1993; Cayatte et al. 1994; Veilleux et al. 1999) and the stripped gas forms sufficient column density to the central source, it would also work as an X-ray reflector, albeit ram-pressure stripping is not expected to be efficient near the centre of a galaxy.

Much of the hard X-ray tail in the southern cone spectrum can be accounted for by the faint wing of the PSF for the nuclear source, although a faint extension is present at the inner part of the western edge of the cone, on inspecting the 4–7 keV image. The hard X-ray spectrum lacks a strong Fe K emission line (Fig. 10). The 90 per cent upper limit on the EW of a narrow line at 6.4 keV is still consistent with the spectral shape of the nuclear source (Section 3.1). A higher-energy line, e.g. at 6.7 keV, appears to be more favoured by the data (in this case, the EW could be around 800 eV), although the significance of the line is sensitive to the assumed underlying continuum. This line may arise from the high ionization gas ($\log \xi \sim 3$) in agreement with the soft X-ray emission (Section 4.1).

5.2 Extended Fe Kα emission

The Fe Kα emitting region is spatially resolved in the *Chandra* image. A narrow-band (6.2–6.5 keV) image centred on cold iron Kα emission is shown in Fig. 11. While much of the line emission arises from the nuclear region, the image of the low surface brightness emission shows ridges extending to the northeast and northwest. A faint extension appears to be present to the north up to 30 arcsec (2.5 kpc). The reality of this extended line emission is supported by the hard X-ray emission with an asymmetric extension examined in the previous subsection (Fig. 9) and the spectrum of the low surface brightness region (LSB in Fig. 10) which shows a strong Fe Kα line with EW much larger than that of the nuclear spectrum. The energy of the line centroid ($\simeq 6.4$ keV) of the LSB spectrum implies that the line emission originates in low ionization gas. The extension of the line emission is in rough agreement with the photoionized gas traced by soft X-ray emission, although any detailed correlation
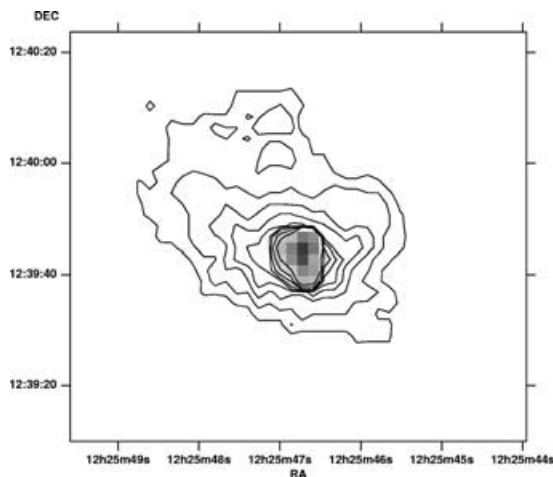

Figure 11. The Fe Kα band (6.2–6.5 keV) image of NGC 4388. The narrow-band image with 2-arcsec binning has been smoothed and the contours of eight logarithmic intervals in the range of 0.05–3 per cent of the peak brightness (at the nucleus position) are superposed to show low surface brightness morphology.

between the two emission components is unclear due to the low signal-to-noise ratio of the Fe Kα emission data.

The 6.4-keV Fe Kα line is a reliable indicator of cold gas, and could trace the history of nuclear activity by mapping the iron line emission (Fabian 1977). The extension of the line emission implies that the central source was turned on at least 10 000 yr ago. More details could be obtained from a deeper observation.

6 DISCUSSION

The soft X-ray image shows clear bi-conical extended emission, bearing a strong resemblance to the optical [O III] ionization cone. The faintness of the northern cone is probably due to the effect of shadowing by the stellar disc on the near side (see Section 4.2). The spatial correlation between the soft X-ray and optical-line emission, which was not found in the much lower signal-to-noise ratio image taken by the *ROSAT* HRI (Matt et al. 1994), suggests a common mechanism working for the creation of the extended nebula. As discussed in Section 4.1, the extended X-ray emission in NGC 4388 is unlikely to be thermal (collisionally ionized) emission from a shock-heated medium, as previously thought (however, Netzer, Turner & George 1998, explained the *ASCA* spectrum with a photoionization model). Convincing evidence for photoionized gas that is responsible for the soft X-ray emission in other type 2 Seyfert galaxies has been obtained from high-resolution spectroscopy with the *XMM–Newton* RGS and the *Chandra* LETG (Ogle et al. 2000; Sako et al. 2000; Brinkman et al. 2002; Kinkhabwala et al. 2002; see also Young, Wilson & Shopbell 2001). This also seems to be the case for the X-ray nebula around NGC 4388.

The strong O VII emission, together with the other low-energy X-ray emission features, found in the spectrum of the southern cone (Fig. 4) suggests that photoionized gas with a low ionization parameter ($\log \xi \sim 0.4$) dominates the bright soft X-ray emission. With the inferred low ionization, the same gas could explain the optical [O III] luminosity, since photoionization codes predict the luminosity ratio of [O III] $\lambda 5007$ to O VII (0.55 keV) to be $\sim$40 for the ionizing spectrum we assumed (this value is from XSTAR). Given the rough power-law approximation to the shape of the ionizing spectrum for the photoionization calculation and various uncertainties, including the aperture difference and varying absorption/extinction across the region, which complicate any direct comparison, the observed line flux ratio [1.2×10^{-12} erg cm^{-2} s^{-1} for [O III] measured with a 12-arcsec aperture by Falcke et al. (1998); 1.8×10^{-14} erg cm^{-2} s^{-1} for O VII measured only from the southern cone] is in rough agreement with the prediction. Recall that the ξ value quoted above is for the inner edge of a photoionized gas shell in the calculation of XSTAR (see Section 4.1), and the ionization parameter varies across the gas: O VII peaks near the inner edge while O III peaks at outer radii, where ξ is lower but the radial emissivity of the two have a significant overlap.

In the southern cone, a comparison between the spectra of the inner and outer parts suggests the ionization parameter is approximately constant with radius (Section 4.1). This implies that the radial density profile follows $n \propto R^{-2}$. Since the same temperature (a few 10^4 K here) should hold for gas with the same ionization parameter, the pressure profile is also proportional to the inverse square of the radius. These dependencies are consistent with gas expanding at constant velocity, ejected matter from the active nucleus, for instance.

If the X-ray nebula around NGC 4388 is indeed photoionized gas, as we demonstrated, its size of over 10 kpc is larger than other photoionized nebulae known around nearby Seyfert galaxies.

High-resolution X-ray spectroscopy is desirable to confirm the photoionization nature. The large extent of the X-ray emission would make a *Chandra* grating observation difficult. An observation with the *XMM–Newton* RGS may still be possible, given the broader PSF of the *XMM–Newton* telescopes. Note, however, such a grating observation will lose information on the spatial variation of gas properties, as we see in the *Chandra* data.

Large-scale X-ray nebulae with the sizes up to a few tens of kpc, which are often associated with Hα emission (e.g. Heckman et al. 1996; Lira et al. 2002), are usually attributed to thermal emission heated by starburst-driven winds (e.g. Lehnert, Heckman & Weaver 1999; Gallagher et al. 2002; Done et al. 2003). However, at least in the presence of an active nucleus, the possibility of photoionized gas as a source of an extended X-ray nebula should be considered, especially when there is a correlation with high ionization optical emission gas such as [O III] λ5007, as seen in NGC 4388.

While the radial extent of the southern cone is limited, the question arises as to why the extension of the gas to the north is so much larger in both optical and X-rays. Various possibilities for the origin of this gas have been proposed: ram-pressure stripping of the interstellar medium (Petitjean & Durret 1993; Veilleux et al. 1999), debris of a small accreted galaxy (Yoshida et al. 2001) and a starburst-driven superwind (e.g. Corbin et al. 1988). The last possibility is not favoured because the X-ray spectrum is not thermal (see also Veilleux et al. 1999; Vollmer & Huchtmeier 2003). The extended cold iron K emission rather favours a photoionization model. The narrow filaments of a few tens of kpc length, imaged by SUBARU, are certainly suggestive of the merger debris hypothesis. They are reminiscent of the tidal tails often observed in a major merger system, e.g. in H I. Of course, the unusual environment particular to NGC 4388, residing in the cluster core and moving at high velocity in it, may play an important role in causing the long one-sided matter distribution.

The radio images show that radio-emitting plasma extends to the north at large radii, whereas the axes of the ionization bi-cone and bright radio emission lie along the NE–SW direction. Veilleux et al. (1999) attributed this misalignment to buoyancy or refractive bending (note that the NE extraplanar ionized gas is moving towards us and the axis of the ionization cone is not perpendicular to the stellar disc). As we noted in Section 4.2, the major axis of the 1–3 keV (green colour in Fig. 1) or 1–2 keV (Fig. 5) emission, which is likely to trace the path of the nuclear radiation at inner radii (within 1 kpc), lies in the NE–SW direction. Its southern extension also matches the well-defined edge of the western side of the southern soft X-ray/O III cone. The fact that the eastern edge of the southern cone is more blurred suggests that some buoyancy effect might bring the ionized gas southwards, while the true axis of the nuclear radiation, which escapes from the nuclear obscuring torus is indicated by the 1–3 keV elongation. In this case, although the apparent opening angle of the southern cone is about 55°, the nuclear ionizing radiation could be more collimated. On the north side, both the 1–2 keV X-ray-emitting gas and radio plasma point towards the NE at small radii and bend towards the north at ∼3 arcsec from the nucleus.

NGC 4388 is often believed to be interacting strongly with the Virgo ICM at supersonic speeds. A Mach cone formed on the far side of the galaxy with an opening angle of ∼80° has been proposed by Veilleux et al. (1999). Some temperature rise in the bowshocked region around the interaction point is expected above that of the surrounding ICM, which should have a temperature of $kT \sim$ 2 keV. Unfortunately, we were unable to find such a bow-shocked region, mainly due to the presence of the extended ionized gas.

The lack of evidence for strong interaction with the ICM leaves room for the hypothesis that NGC 4388 could be more distant than the Virgo cluster and lies closer to its Hubble distance for $cz = 2540$ km s^{-1}.

Finally, with regard to the unification scheme of the two types of Seyfert galaxies, if the nucleus of NGC 4388 were viewed from a direction near the axis of the ionization cone, the central X-ray source would be seen through the low ionization gas (and possibly very high ionization gas). The column density of the low ionization gas could be of the order of 10^{22} cm^{-2}, depending on the filling factor. Although the detailed X-ray grating spectra of bright type 1 Seyfert galaxies, such as NGC 3783 (Kaspi et al. 2002), do not show clear evidence for such low ionization gas, it might be seen in other mildly absorbed Seyfert nuclei.

ACKNOWLEDGMENTS

REFERENCES

Bassani L., Dadina M., Maiolino R., Salvati M., Risaliti G., Della Ceca R., Matt G., Zamorani G., 1999, ApJS, 121, 473
Brinkman A.C., Kaastra J.S., van der Meer R.L.J., Kinkhabwala A., Behar E., Kahn S.M., Pearels F.B.S., Sako M., 2002, A&A, 396, 761
Carral P., Turner J.L., Ho P.T.P., 1990, ApJ, 362, 434
Cayatte V., Kotanyi C., Balkowski C., van Garkum J.H., 1994, AJ, 107, 1003
Chamaraux P., Balkowski C., Gérard E., 1980, A&A, 83, 5
Chevalier R.A., Clegg A.W., 1985, Nat, 317, 44
Ciroi S., Contini M., Rafanelli P., Richter G.M., 2003, A&A, 400, 859
Colina L., 1992, ApJ, 386, 59
Colina L., Fricke K.J., Kollatschny W., Perryman M.A.C., 1987, A&A, 186, 39
Corbin M.R., Baldwin J.A., Wilson A.S., 1988, ApJ, 334, 584
Davis J.E., 2001, ApJ, 562, 575
Dickey J.M., Lockman F.J., 1990, ARA&A, 28, 215
Done C., Madejski G.M., Życki P., Greenhill L.J., 2003, ApJ, 588, 763
Fabian A.C., 1977, Nat, 269, 672
Falcke H., Wilson A.S., Simpson C., 1998, ApJ, 502, 199
Filippenko A.V., Sargent W.L.W., 1985, ApJ, 57, 503
Ford W.K., Rubin V.C., Roberts M.S., 1971, AJ, 76, 22
Forster K., Leighly K.M., Kay L.E., 1999, ApJ, 523, 521
Gallagher S.C., Brandt W.N., Chartas G., Garmire G.P., Sambruna R.M., 2002, ApJ, 569, 655
Giovanelli R., Haynes M.P., 1983, AJ, 88, 881
Hanson C.G., Skinner G.K., Eyles C.J., Wilmore A.P., 1990, MNRAS, 242, 262
Heckman T.M., Dahlem M., Eales S.A., Fabbiano G., Weaver K.A., 1996, ApJ, 457, 616
Hummel E., Saikia D.J., 1991, A&A, 249, 43
Iwasawa K., Fabian A.C., Ueno S., Awaki H., Fukazawa Y., Matsushita K., Makishima K., 1997, MNRAS, 285, 683
Kaastra J.S., 1992, An X-Ray Spectral Code for Optically Thin Plasmas. Internal SRON-Leiden Rep., updated version 2.0
Kallman T., Bautista M., 2001, ApJS, 133, 221
Kaspi S. et al., 2002, ApJ, 574, 643
Kay L.E., 1994, ApJ, 430, 196
Kenney J.D., Young J.S., 1986, ApJ, 301, L13
Kinkhabwala A. et al., 2002, ApJ, 575, 732
Kinney A.L., Antonucci R.R.J., Ward M.J., Wilson A.S., Whittle M., 1991, ApJ, 377, 100

Koyama K., Maeda Y., Sonobe T., Takeshima T., Tanaka Y., Yamauchi S., 1996, PASJ, 48, 249

Lehnert M.D., Heckman T.M., Weaver K.A., 1999, ApJ, 523, 575

Lira P., Ward M.J., Zezas A., Murray S.S., 2002, MNRAS, 333, 709

Matt G., Piro L., Antonelli L.A., Fink H.H., Meur E.J.A., Perola G.C., 1994, A&A, 292, L13

Netzer H., Turner T.J., George I.M., 1998, ApJ, 504, 680

Ogle P.M., Marshall H.L., Lee J.C., Canizares C.R., 2000, ApJ, 545, L81

Petitjean P., Durret F., 1993, A&A, 277, 365

Phillips M.M., Malin D.F., 1982, MNRAS, 199, 905

Pogge R.W., 1988, ApJ, 332, 702

Ross R.R., Fabian A.C., Young A.J., 1999, MNRAS, 306, 461

Sako M., Kahn S.M., Paerels F., Liedahl D.A., 2000, ApJ, 543, L115

Sandage A., 1978, AJ, 83, 904

Shields J.C., Filippenko A.V., 1988, ApJ, 332, L55

Stone J.L., Wilson A.S., Ward M.J., 1988, ApJ, 330, 105

Veilleux S., Bland-Hawthorn J., Cecil G., Tully R.B., Miller S.T., 1999, ApJ, 520, 111

Vollmer B., Huchtmeier W., 2003, A&A, 406, 427

Weisskopf M.C., Tananbaum H.D., Van Speybroeck L.P., O'Dell S.L., 2000, in Trümper J.E., Aschenbach B., eds, Proc. SPIE, Vol. 4012, X-ray optics, Instruments, and Missions III. Int. Soc. Opt. Eng., Bellingham, WA, p. 2

Yoshida M. et al., 2001, ApJ, 567, 118

Young A.J., Wilson A.S., Shopbell P.L., 2001, ApJ, 556, 6

APPENDIX

Detector-efficiency-corrected versions of spectral data shown in Figs 2, 4 and 10 are presented below in Figs A1–3. The count rate spectra have been divided by the effective area. The correction is independent of the fitted model but some uncertainty may have been introduced due to the detector resolution and data binning. The time-dependent efficiency degradation in the low-energy range specific to the ACIS-S3 detector, which was taken into account by ACISABS in the spectral analysis, has also been included.
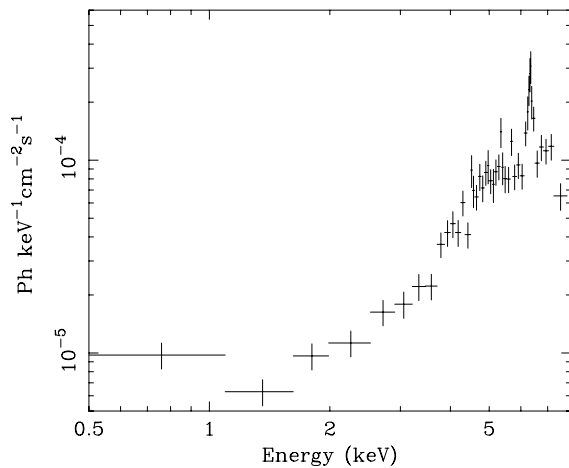

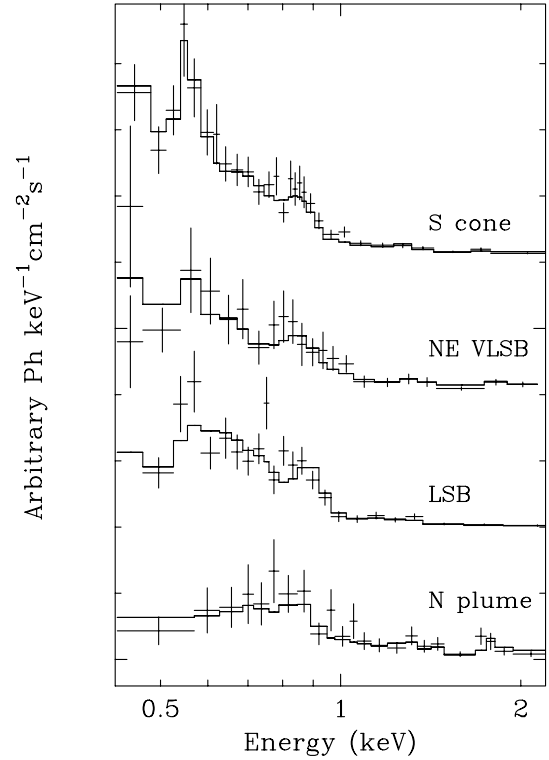**Figure A1.** The same figures as Fig. 2 but corrected for the detector efficiency.

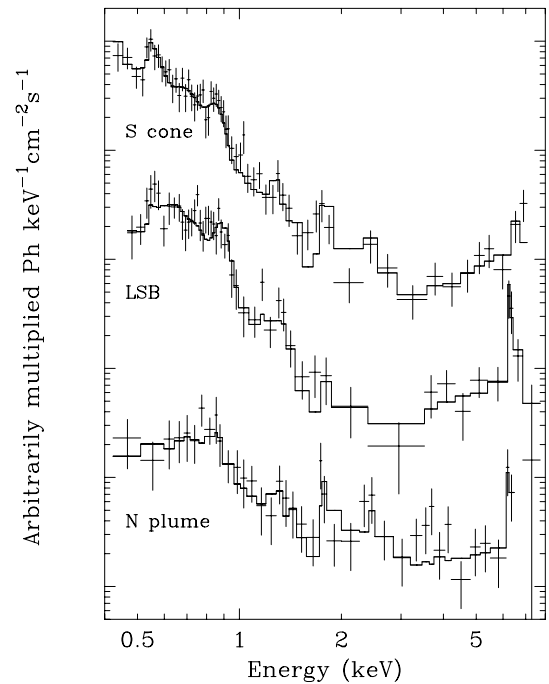**Figure A2.** The same figures as Fig. 4 but corrected for the detector efficiency.

Figure A3. The same figures as Fig. 10 but corrected for the detector efficiency.

This paper has been typeset from a TEX/LATEX file prepared by the author.